Doppler-shift attenuation lifetime measurement of the ^{36}Ar 2_1^+ level

P. Voss,[1,2,*] T. E. Drake,[3] K. Starosta,[1,†] C. Andreoiu,[1] R. Ashley,[1] G. C. Ball,[4] P. C. Bender,[4] A. Chester,[1] R. Churchman,[4] D. S. Cross,[1] A. B. Garnsworthy,[4] G. Hackman,[4] B. Hadinia,[5] R. Henderson,[4] B. Jigmeddorj,[5] S. Ketelhut,[4] R. Krücken,[4,6] A. T. Laffoley,[5] K. G. Leach,[5,‡] D. Miller,[4] R. Orlandi,[7] C. J. Pearson,[4] J. Pore,[1] M. M. Rajabali,[4] E. T. Rand,[5] C. E. Svensson,[5] E. Tardiff,[4] C. Unsworth,[4] Z.-M. Wang,[1,4] and A. Signoracci[8,9]

[1]*Department of Chemistry, Simon Fraser University, Burnaby, British Columbia V5A 1S6, Canada*
[2]*Department of Physics, Albion College, Albion, Michigan 49224, USA*
[3]*Department of Physics, University of Toronto, Toronto, Ontario M5S 1A7, Canada*
[4]*TRIUMF, 4004 Wesbrook Mall, Vancouver, British Columbia V6T 2A3, Canada*
[5]*Department of Physics, University of Guelph, Guelph, Ontario N1G 2W1, Canada*
[6]*Department of Physics, University of British Columbia, Vancouver, British Columbia V6T 1Z4, Canada*
[7]*Institutos del CSIC, Instituto de Estructura de la Materia, Madrid, 28006, Spain*
[8]*Physics Division, Oak Ridge National Laboratory, Oak Ridge, Tennessee 37831, USA*
[9]*Department of Physics and Astronomy, University of Tennessee, Knoxville, Tennessee 37996, USA*

(Received 13 April 2017; revised manuscript received 28 June 2017; published 11 August 2017)

At TRIUMF, the TIGRESS Integrated Plunger device and its suite of ancillary detector systems have been implemented for charged-particle tagging and light-ion identification in coincidence with γ-ray spectroscopy for Doppler-shift lifetime studies and low-energy Coulomb excitation measurements. As a test of the device, the lifetime of the first 2^+ excited state in ^{36}Ar was measured from the γ-ray line shape of the $2_1^+ \rightarrow 0_{g.s.}^+$ transition using the Doppler-shift attenuation technique following Coulomb excitation. The line-shape signatures, vital for precision lifetime measurements, were significantly improved by enhanced reaction-channel selectivity using a complementary approach of kinematic gating and digital rise-time discrimination of recoiling charged particles in a silicon PIN diode array. The lifetime was determined by comparisons between the data and simulated line shapes generated using our TIGRESS Coulomb excitation code as an input to the Lindhard method, which was then extended and included as a class in GEANT4. The model-independent lifetime result of 490 ± 50 fs corresponds to a reduced quadrupole transition strength of $B(E2; 2_1^+ \rightarrow 0_{g.s.}^+) = 56 \pm 6$ e^{2}fm^4 and agrees well with previous intermediate energy Coulomb excitation measurements, thereby resolving reported discrepancies in the 2_1^+ level lifetime in this self-conjugate nucleus.

DOI: 10.1103/PhysRevC.96.024305

I. INTRODUCTION

Sensitive experimental devices and techniques are required to study the properties of radioactive atomic nuclei at the extremes of isospin since the signal-to-noise ratio of observables is inherently low. The progression of experimental capabilities is therefore paramount for uncovering interesting nuclear phenomena in systems across the chart of nuclides. Some of these include the unconventional ordering of shell-model orbitals such as the inverted ground-state parity structure in ^{11}Be [1–3] and the intruder orbital configurations in neutron-rich $N \sim 20$ "island of inversion" isotopes [4,5]; the coexistence of competing nuclear shapes with nearly degenerate energies such as proton-rich ^{186}Pb [6] and neutron-rich $N \sim 60$ Sr and Zr isotopes [7,8]; and the rapid evolution and competition of nuclear shapes in mid-pf shell $N = Z$ nuclei [9–13]. Electromagnetic transition rate measurements play an important role in these investigations and have been used to systematically characterize the evolution of nuclear structure with increasing proton-neutron asymmetry. They are therefore useful in vetting a wide variety of theoretical models developed for broad applicability over the nuclear landscape.

As part of this effort, the TIGRESS Integrated Plunger (TIP) device [14] has been developed for transition rate measurements—key pieces of information in accessing nuclear shape information—via both excited-state lifetime [15,16] and low-energy Coulomb excitation [17] experiments. TIP combines multiple targetry and ancillary charged-particle detection options with high-precision γ-ray spectroscopy using the TRIUMF-ISAC Gamma-Ray Escape Suppressed Spectrometer (TIGRESS) [18–21]. This combination provides reaction-channel selectivity and precision kinematic information following a variety of experimental reaction mechanisms, enhancing the sensitivity of γ-ray energy line-shape signatures for nuclear structure investigations.

In this work, we present the in-beam lifetime measurement of the 2_1^+ excited state in self-conjugate ^{36}Ar as the first test of transition rate studies with TIGRESS and the TIP silicon PIN diode array. The measurement was completed using the Doppler-shift attenuation method (DSAM) lifetime technique [15] following inelastic excitation in inverse kinematics (cf. Ref. [22] for a similar experimental setup). This combination of techniques is appealing; lifetime measurements

*Electronic address: pvoss@albion.edu; office phone: 517-629-0478.
†Electronic address: starosta@sfu.ca; office phone: 778-782-8861.
‡Present address: Department of Physics, Colorado School of Mines, Golden, CO 80401, USA.

TABLE I. Reduced quadrupole transition rate and lifetime values for the first 2^+ excited state in ^{36}Ar. All transition strengths in this work will be quoted as $B(E2\downarrow)$ values. The literature value is taken from the compilation of Ref. [28] as it predates the results we compare; it is a weighted average of previous DSAM and low-energy Coulomb excitation measurements.

Ref.	Method	$B(E2)$ (e^2fm^4)	τ (fs)
[28]	Literature value	68.0 ± 8.0	404 ± 48
[25]	Int. energy Coul. exc.	57.2 ± 4.6	480 ± 39
[26]	Int. energy Coul. exc.	62.0 ± 6.2	443 ± 44
[27]	DSAM lifetime	42.3 ± 1.3	650 ± 20
[27]	Shell model calc.	64.4	427

yield a model-independent measure of transition probabilities regardless of the chosen reaction mechanism, absolute cross section, or beam energy while Coulomb excitation reliably populates the state of interest. Moreover, if the beam energy is chosen to be "safe"—that is, below the Coulomb barrier to avoid nuclear contributions to the excitation at the expense of the overall reaction rate—the diagonal nuclear matrix elements and their signs, which carry direct shape information, can also be extracted. Elsewhere, we have reported on DSAM lifetime measurements following fusion-evaporation reactions using TIGRESS and the TIP CsI(Tl) scintillator array [23].

The scientific aim of this study was to resolve reported discrepancies in the reduced quadrupole transition strength, $B(E2; 2_1^+ \rightarrow 0_{g.s.}^+)$, between two previous intermediate energy Coulomb excitation [24] studies [25,26] and a more recent DSAM lifetime measurement [27]. In the DSAM measurement, transition rates and g factors in ^{36,38}Ar and ^{32}S were compared to sd shell-model calculations. The measured and calculated values agreed well—suggesting excitations into the pf shell were unnecessary to describe these systems—except for the $B(E2; 2_1^+ \rightarrow 0_{g.s.}^+)$ in ^{36}Ar, where the experimental value was significantly smaller than both the calculations and the prevailing adopted literature value [28]. In contrast, the intermediate energy Coulomb excitation studies produced results similar to the calculations of Ref. [27] and in agreement with the literature. Table I presents a comparison of these lifetimes and associated $B(E2)$ values.

The argon isotopic chain has been a rich field for study. Along the proton drip line, ^{31}Ar was found to exhibit the exotic $\beta 3p$ decay mode [29]. For the neutron-rich even-even isotopes, large-scale shell-model calculations reproduced the measured $B(E2)$ in ^{48}Ar [30] and ^{50}Ar [31]—indicating an $N = 32$ subshell closure analogous to those observed in neighboring Ca and Ti isotopes—while overestimating the collectivity in ^{46}Ar. This is puzzling, as both $B(E2)$ data from Coulomb excitation [32–34] and mass measurements [35] point to a robust $N = 28$ shell closure for $Z = 18$. Even at stability, superdeformation has been observed in ^{36}Ar with a very low bandhead energy of only 4.3 MeV [36,37] and has been well described by theory [38]. For this self-conjugate system, two neutrons (protons) shy of $N(Z) = 20$, it is reasonable to anticipate agreement between data and shell-model calculations without invoking cross-shell excitations into the pf model space. This was demonstrated in Ref. [39], where agreement for the low-lying positive-parity energy levels and $M1$ strength distributions was good within the sd model space. This makes the resolution of the discordant $B(E2)$ measurements in ^{36}Ar and agreement with modern shell-model predictions all the more compelling.

II. EXPERIMENTAL METHOD AND RESULTS

The lifetime measurement was performed at the ISAC-II facility of TRIUMF [40], Canada's national laboratory for particle and nuclear physics. The state of interest was populated by Coulomb excitation of a 1.75 AMeV ^{36}Ar beam on a $0.43\,mg/cm^2(1.9\,\mu m)$ carbon target evaporated onto a $22.2\,mg/cm^2(11.5\,\mu m)$ gold backing [41]. The target was mounted at the center of the TIP scattering chamber, which was enclosed within 13 TIGRESS clover detectors at a radial distance of 14.5 cm from the target position in the optimized peak-to-total configuration [42]. The forward and backward clover positions, with average polar angles with respect to the beam axis of 45° and 135°, respectively, were fully populated with four clovers each. An additional five clovers were placed at 90°. Subdividing each clover into two pairs of crystals results in six TIGRESS rings centered at unique polar angles of 35°, 55°, 80°, 100°, 125°, and 145°. Both TIGRESS clover and TIGRESS ring spectra were used in the analysis presented below.

γ rays were detected with TIGRESS in coincidence with particles in the 44-element TIP silicon PIN diode array. All data were digitized synchronously using the 100-MHz, 14-bit ADCs of the TIGRESS data acquisition (DAQ) system [43] utilizing a 1-μs coincidence trigger window. The silicon array was installed 63.9 mm downstream from the DSAM target with the individual detectors organized into four rings of similar laboratory polar angles with respect to the beam axis: 14.4°, 23.1°, 29.0°, and 33.4° for rings 1–4, respectively. This coverage corresponds to backward center-of-mass angles between 95° and 160°. All recoiling charged particles energetic enough to emerge from the gold backing were stopped within the depletion region of the silicon detectors. This, in part, enabled a selective particle-γ DAQ trigger which localized the excitation of ^{36}Ar to the thin carbon layer of the DSAM target, precluding significant γ-ray line-shape contamination from inelastic excitations on the thick gold backing. In addition, time gates were implemented on both the γ-ray and recoiling particle spectra to remove random coincidences from the data as they lack kinematic correlations, thereby obscuring the proper Doppler-shifted line shape. To improve the peak-to-total of γ-ray energy deposits, the full-clover add-back energy summing and suppression schemes for TIGRESS were utilized [44]. Figure 1(a) illustrates the resulting γ-ray energy spectrum for the 45° TIGRESS clover detectors properly correlated with recoiling charged particles in the full TIP silicon PIN diode array.

The transitions from ^{37}Ar (2490.2 and 2108.2 keV, but Doppler shifted to ≈2150 keV), ^{40}Ca (3736.3 and 3904.0 keV), and ^{44}Ti (2093.1 keV) visible in Fig. 1 arise from reaction mechanisms competing with ^{36}Ar inelastic excitation on the carbon layer of the DSAM target: neutron pickup from ^{13}C as well as one- and two-α particle transfer from ^{12}C

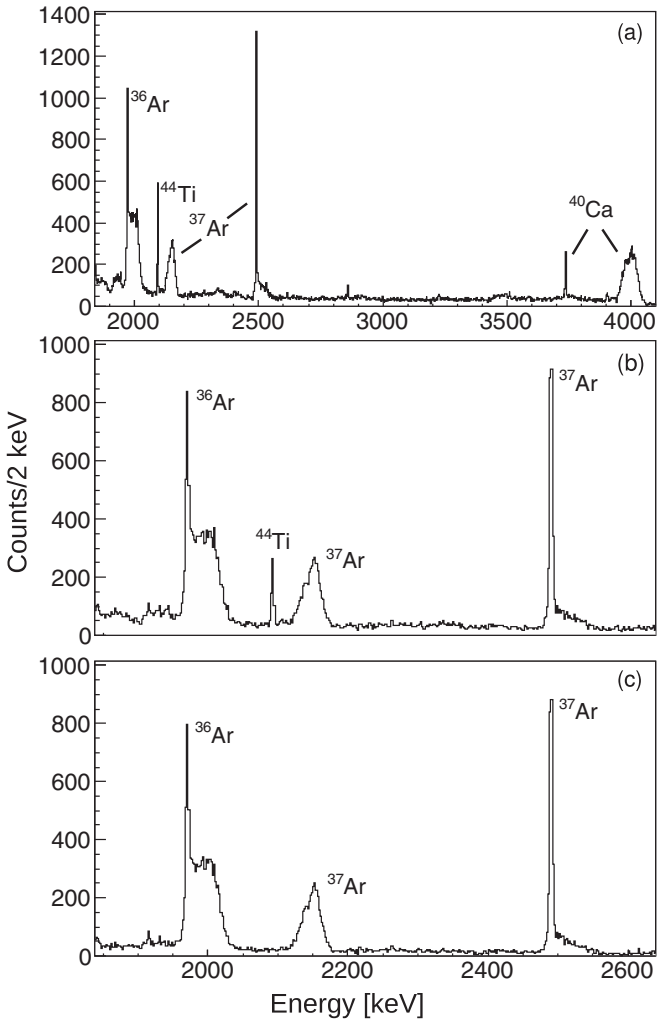

FIG. 1. γ-ray energy spectra detected with the 45° TIGRESS clovers in coincidence with all recoiling charged particles in the TIP silicon PIN diode array in panel (a). The ^{36}Ar $2_1^+ \rightarrow 0^+_{\text{g.s.}}$ transition at 1970.3 keV exhibits well-developed slowing and stopped components. The signal to noise was improved with kinematic suppression as demonstrated in panel (b)—like panel (a), but only γ rays in coincidence with recoiling charged particles in rings 1 and 2 of the silicon array—and silicon rise-time discrimination as demonstrated in panel (c)—like panel (b), but with the additional requirement that particles have carbon-like rise times in the silicon array (cf. Fig. 2).

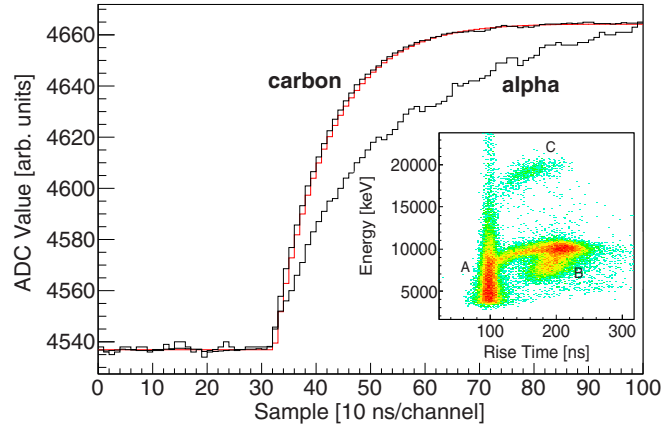

FIG. 2. Two representative 1-μs wave-form traces (black) from the TIP silicon PIN diode array, normalized with baselines aligned. The rise times of the traces corresponding to carbon and α particles are 98 and 212 ns, respectively, and are extracted from event-by-event fits; the best-fit function (red) to the carbon wave form is overlaid atop the data. The resulting particle identification from silicon DRD is demonstrated in the inset, where the incident ion energy is plotted against the extracted rise time for recoils detected in ring 2 of the silicon array. The three distinct regions A, B, and C correspond to the detection of carbon, one α particle, and two α particles in a single photodiode, respectively. Only γ rays in coincidence with particles in region A from the silicon array rings 1 and 2 were used in the line-shape analysis to extract the ^{36}Ar 2_1^+ lifetime.

breakup, respectively. The Compton continuum from these intense, high-energy transitions impact the signal to noise of the Doppler-shifted line shape of the ^{36}Ar $2_1^+ \rightarrow 0^+_{\text{g.s.}}$ transition of interest. Therefore, to enhance the sensitivity of the line shape to lifetime effects, the PIN diode array data were used in two complementary ways. First, only γ rays in coincidence with recoils in the innermost two PIN diode array rings were used for the lifetime analysis since very few carbon target recoils from the inelastic excitation of ^{36}Ar were energetic enough to exit the DSAM target gold backing at angles $\gtrsim$25°, corresponding to rings 3 and 4. γ rays in coincidence with these outermost two rings resulted from α-transfer contaminant reactions. This kinematic gate reduced the contribution of these reactions to the γ-ray line-shape data as illustrated by the intensity reduction of the $3_1^- \rightarrow 2_1^+$ ^{44}Ti transition at 2093.1 keV from Fig. 1(a) to Fig. 1(b). Next, the digitized silicon PIN diode wave-form traces from rings 1 and 2 were fit on an event-by-event basis to separate α-like and carbon-like rise times as discussed in detail in Ref. [45]. Figure 2 demonstrates the significant rise-time differences between these two types of events. This digital rise-time discrimination (DRD) effectively removed the remaining α-transfer contaminant reaction contributions from the line-shape data as evidenced by the complete removal of the ^{44}Ti transition from Fig. 1(b) to Fig. 1(c). Figure 1(c) depicts the subset of γ-ray data in coincidence with particles with carbon-like rise times in rings 1 and 2 that were retained for analysis.

The enhanced Doppler-shifted line shape of the ^{36}Ar $2_1^+ \rightarrow 0^+_{\text{g.s.}}$ transition as given in Fig. 1(c), containing both slowing and fully stopped de-excitation components, together with information about the beam energy and the DSAM target thickness and stopping powers, is sufficient to precisely determine lifetimes on the order of a several hundred femtoseconds. In contrast, the two ^{37}Ar transitions in Fig. 1 exhibit more homogeneous line shapes due to lifetimes both smaller and larger; the $3/2_2^- \rightarrow 1/2_1^+$ transition at 2108.2 keV ($\tau = 59(35)$ fs [46]) is fully shifted while the $3/2_1^- \rightarrow 3/2_1^+$ transition at 2490.2 keV ($\tau = 667(160)$ fs [46]) is mostly stopped. Thus, to extract the lifetime of the 2_1^+ excited state, ^{36}Ar line shapes were compared with Monte Carlo γ-ray line-shape simulations using several approaches.

III. SIMULATIONS AND ANALYSIS

The best-fit lifetime was extracted using line-shape simulations fit to the experimental data. In the simulations, a beam of ^{36}Ar impinged upon a DSAM target and was Coulomb excited on the carbon reaction layer. Both the scattered ^{36}Ar projectiles and the recoiling carbon ions were propagated into the gold backing layer. The excited ^{36}Ar were slowed to a stop in the backing, emitting γ rays. The resulting line shapes depended upon the projectile momenta, the angle of γ-ray detection, and the stopping power of the backing; therefore care was taken to reproduce the experimental details in the simulations. The position, composition, and sizes of the TIGRESS clover detectors, the TIP silicon PIN diode array, and the DSAM target were input into the simulations to yield the proper geometric efficiencies. We incorporated the Coulomb excitation reaction mechanism in inverse kinematics. In addition, we investigated uncertainties in both our choice of stopping powers and the thickness of the DSAM target gold backing to preserve the proper kinematic and energy correlations.

We have pursued two independent methods of γ-ray energy line-shape simulations, checking them against one another and the experimental data. In the first of these methods, we adopted the Lindhard formalism as described in Ref. [47], where multiple nuclear scattering and stopping are modeled in a Monte Carlo technique as a random process above a smooth background of electronic stopping. The latter contribution slows heavy ions without deflection and was implemented using SRIM stopping powers [48]. The projectile propagates in this manner through successive nuclear deflections, which become more dominant as the kinetic energy is reduced. The slowing process, smoothed via averaging over many trials, is then folded with the lifetime dependence for γ-ray emission, yielding γ-ray line shapes for each simulated lifetime. The original stopping codes were obtained from the Oak Ridge Wells and Johnston compilation [49]; we altered them to include the Coulomb excitation process for the production of the scattered excited projectile and target recoil in inverse kinematics and incorporated them into our own line-shape programs.

In the second method, we adopted GEANT4 Monte Carlo simulations [50] for line-shape generation, but replaced the Urban standard multiple scattering and energy loss classes [51] with the aforementioned Lindhard formalism of projectile stopping. This substitution was done as the standard GEANT4 classes for multiple scattering produced line shapes in poor agreement with our data. We used the TIGRESS clover detector GEANT4 class, as originally reported in Ref. [42], and modified classes to be relevant for the propagation of ions in the energy range of the present experiment. Other classes were written for Coulomb excitation and radiative decay and incorporated with the pertinent TIP experimental devices into the GEANT4 code.

A. Line-shape simulations: Method I

Our own line-shape simulations within the Lindhard formalism utilized a simplified cylindrical geometry for the TIGRESS crystals, which were grouped into common TIGRESS ring angles. Like the experimental data, only simulated γ rays

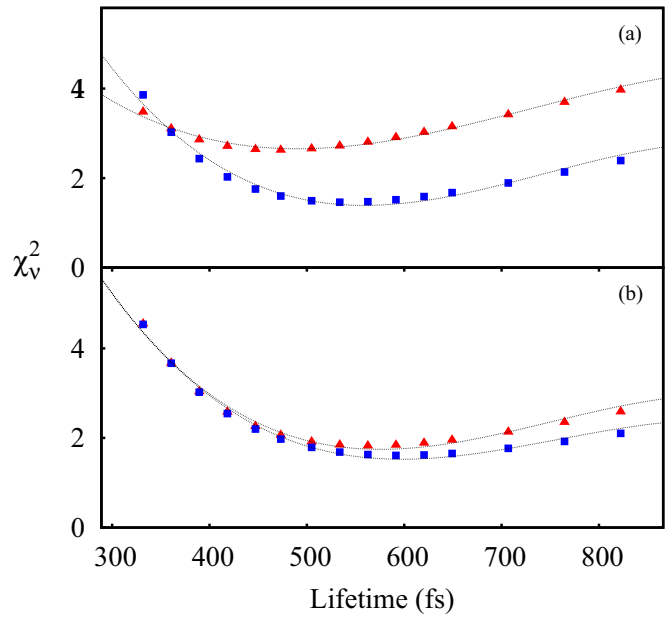

FIG. 3. Distributions of reduced-χ^2 values as a goodness-of-fit test between simulations and experimental data for backward TIGRESS rings of 145° (blue squares) and 125° (red triangles) in panel (a) and forward TIGRESS rings of 55° (blue squares) and 35° (red triangles) in panel (b).

in coincidence with carbon recoils detected in rings 1 and 2 of the PIN diode array were used in the analysis. Line shapes were generated as a function of lifetime in steps of 30–60 fs. For each lifetime simulation step, the area of the simulated line shape was normalized to the area of the experimental counterpart before comparing them with a χ^2 goodness-of-fit test. Distributions of reduced-χ^2 values from the fit of these simulations to the experimental data for the Doppler-shift sensitive TIGRESS rings at 35°, 55°, 125°, and 145° are shown in Fig. 3 along with cubic-polynomial fits. From the minima of these fits, we extracted a weighted average lifetime of 557 ± 17 fs. The statistical errors for each distribution were taken from the average half width of the cubic polynomials evaluated at $\chi^2_\nu = \chi^2_{\nu,\mathrm{min}} + 1/\nu$, where ν is the number of degrees of freedom; we have taken the largest of these as the quoted statistical uncertainty. Adding a 10% stopping powers uncertainty in quadrature, we arrive at a result of 557 ± 58 fs.

We have pursued another goodness-of-fit measure by comparing the integrated counts in the stopped peak and shifted plateau for the experimental and normalized simulated line shapes. The integration of the stopped peak and shifted plateau was done over the energy intervals of [1965,1978] keV and [1913,1964] keV (backward TIGRESS rings), and [1965,1978] keV and [1980,2030] keV (forward TIGRESS rings), respectively. From these integrated counts, we constructed the ratio $\mathcal{R} = \mathcal{R}_{\mathrm{stopped}}/\mathcal{R}_{\mathrm{shifted}}$, where $\mathcal{R}_{\mathrm{stopped}} = \mathcal{S}_{\mathrm{stopped}}/\mathcal{E}_{\mathrm{stopped}}$ and $\mathcal{R}_{\mathrm{shifted}} = \mathcal{S}_{\mathrm{shifted}}/\mathcal{E}_{\mathrm{shifted}}$ with $\mathcal{E}$ and $\mathcal{S}$ being the integrated counts of the experimental and normalized simulated line shapes, respectively. $\mathcal{R} = 1$ indicates a good agreement between the normalized simulations and experimental data, whereas a value larger or smaller than

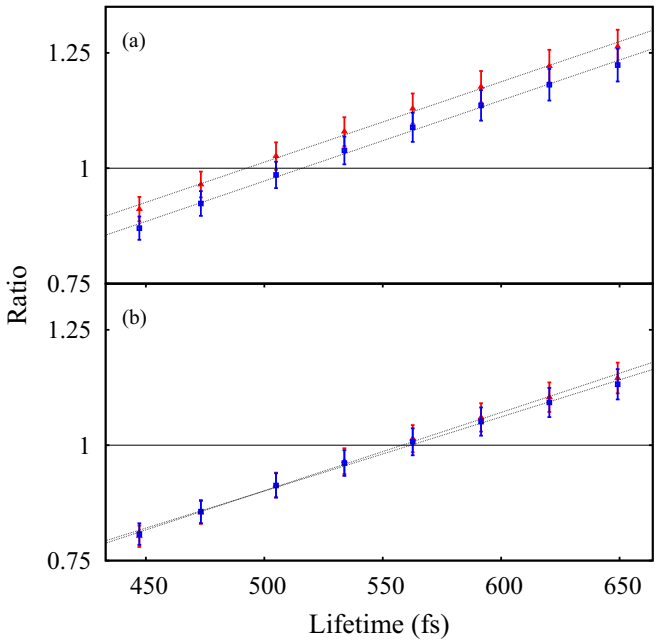

FIG. 4. $\mathcal{R} = \mathcal{R}_{\text{stopped}}/\mathcal{R}_{\text{shifted}}$ as a function of simulated lifetime for backward TIGRESS rings of 145° (blue squares) and 125° (red triangles) in panel (a) and forward TIGRESS rings of 55° (blue squares) and 35° (red triangles) in panel (b).

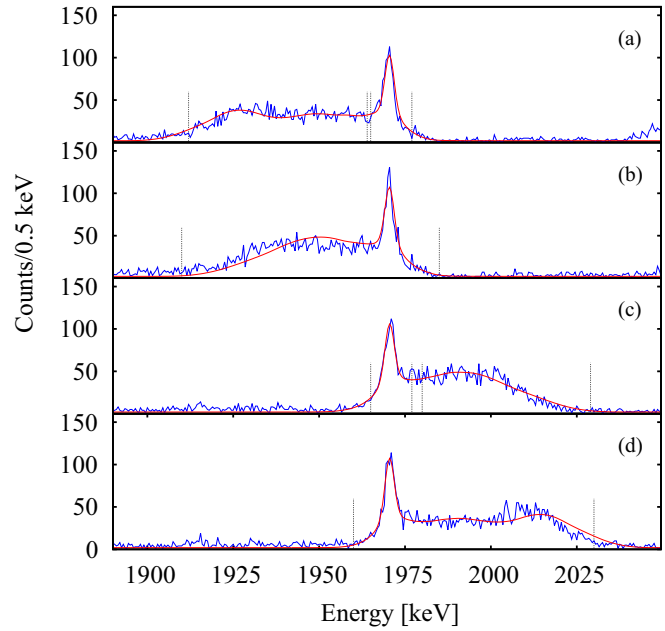

FIG. 5. Experimental (blue) and method I best-fit simulated (red) γ-ray line shapes at four TIGRESS rings: 145° in panel (a), 125° in panel (b), 55° in panel (c), and 35° in panel (d). The simulations have an enforced coincident detection of γ rays and carbon recoils detected in rings 1 and 2 of the TIP silicon PIN diode array. The dashed vertical lines in panels (b) and (d) illustrate the normalization intervals for the simulated line shapes while those in panels (a) and (c) indicate the stopped and shifted intervals for the investigation of $\mathcal{R}$.

1 corresponds to a simulated lifetime too long or too short, respectively.

Figure 4 plots $\mathcal{R}$ as a function of simulated lifetime along with the linear best-fit lines and the horizontal $\mathcal{R} = 1$ lines. The four data sets correspond to the four Doppler-shift sensitive TIGRESS rings. We note the consistency of the results for the 35° and 55° rings, which is reflected in the similar reduced-χ^2 distributions of Fig. 3(b). Similarly, the 24-fs spread of $\mathcal{R} = 1$ results for the 125° and 145° rings is reflected in the location of the minima in the reduced-χ^2 distributions in Fig. 3(a). Taking this spread as a proxy for the statistical error and averaging the $\mathcal{R} = 1$ intersections of the best-fit lines, we deduce a lifetime of 532 ± 24 fs. Adding a 10% stopping powers uncertainty in quadrature, we arrive at a result of 532 ± 58 fs, consistent with the result from the minima in the distribution of χ^2_ν values presented above. Figure 5 illustrates the agreement between the best-fit simulations and data. The dashed vertical lines in Figs. 5(a) and 5(c) indicate the energy intervals of the stopped peak and shifted plateau used in the investigation of the ratio $\mathcal{R}$ in Fig. 4. Those in Figs. 5(b) and 5(d) indicate the energy intervals of [1910, 1985] keV and [1960, 2030] keV, respectively, used for normalization of the simulated line shapes to the experimental data.

B. GEANT4 simulations: Method II

Despite the general consistency of the lifetime results presented above, we note that the distributions of χ^2_ν values in Fig. 3 are rather broad, especially for larger lifetimes. In addition, there is a marked difference in the lifetime at $\mathcal{R} = 1$ for the forward and backward TIGRESS rings as evident in Fig. 4. Lastly, there is a modest discrepancy between the line-shape simulations and experimental data at large Doppler shifts as illustrated best in Fig. 5(b) and 5(d). Thus, the method I results serve as a useful first-pass analysis. To improve upon them and obtain a more accurate and higher precision lifetime result, we have pursued GEANT4 line-shape simulations for an independent lifetime determination. These simulations combined the TIGRESS clover detector GEANT4 class [42] with code written for the TIP silicon PIN diode array and Coulomb excitation reactions in inverse kinematics. The latter determines the event-by-event γ-ray angular correlations and proper projectile and recoil scattering kinematics. We have neglected any deorientation effects in the carbon reaction layer and gold backing layer of the DSAM target as the in-medium interactions change the charge state of the excited projectile rapidly, randomizing any hyperfine interaction perturbations.

An advantage of the GEANT4 simulations is the propagation and tracking of γ rays through the TIGRESS clover detectors. This permitted the add-back summing technique where multiple γ-ray energy deposits within a single clover detector were summed and assigned to the crystal with the largest individual deposit. This assumption has been determined to be robust for γ-ray energies in excess of 500 keV [52], well below our energy range of interest. Thus, the simulations account for both solid angle effects and scattering between neighboring clover crystals in a manner consistent with how the experimental line shapes were constructed, preserving the correct efficiencies.

Another advantage of GEANT4 is the ability to probe various simulation parameters independently in search of

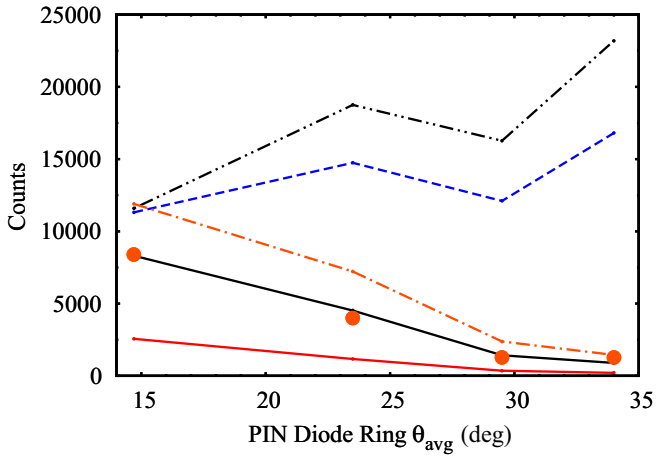

FIG. 6. The normalized experimental γ-ray yields as a function of the TIP silicon PIN diode array ring laboratory polar angle (orange circles) were obtained by summing all TIGRESS clovers in coincidence with carbon recoils in each ring. Simulated TIGRESS yields are plotted in comparison for gold backing thicknesses of infinitely thin (dot-dot-dashed black), 4.5 μm (dashed blue), 9.5 μm (dot-dashed orange), 11.0 μm (solid black), and 13 μm (solid red). The shapes of the simulated yields best agree with the data for gold backing thicknesses between 10 and 12 μm.

best-fit values that improve accuracy. For example, Figs. 6 and 7 highlight some results of investigating the DSAM target gold backing thickness parameter space. Variations in this thickness have an impact on the simulated number of detected carbon recoils, strongly influencing the simulated coincident γ-ray yield as a function of the ring polar angles of the PIN diode array. This is demonstrated in Fig. 6 for five thickness choices with all simulations normalized to the same number of ^{36}Ar inelastic excitations. For thicker

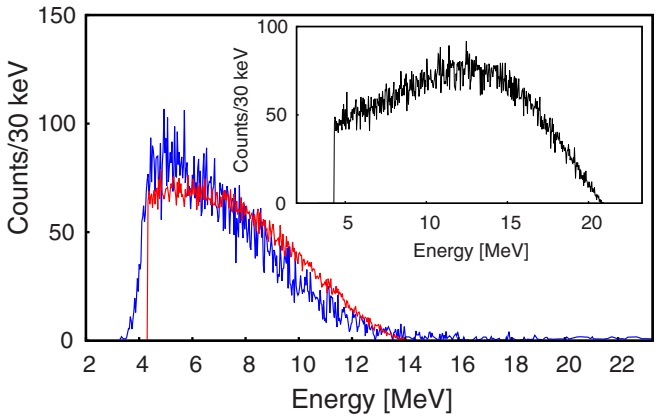

FIG. 7. Experimental (blue) and method II simulated (red) carbon recoil energy spectra from ring 1 of the TIP silicon PIN diode array. An 11.5-μm gold backing thickness was used in the simulations, which also employed a step-function low-energy threshold cutoff as an approximation of the steep experimental energy threshold. For comparison, the inset shows the same simulations with a 9.5-μm gold backing thickness. Notice the significant peak shift to higher energies, away from the experimental result.

backings, the yield falls predictably with increasing carbon recoil angle; as discussed in Sec. II, higher angle recoils were not energetic enough to emerge from the DSAM target gold backing. For thinner backings, the yields are not constrained by stopped carbon recoils and instead increase with laboratory polar angle as the cross section maximum (near 75° in the center of mass) is approached. It is clear that the simulated γ-ray yields using gold backing thicknesses between 10 and 12 μm preferentially fit the shape of the data—shown as orange circles and normalized to the $\theta_{\text{avg}} = 14.4°$ yield from 11.5-μm simulations (not pictured, cf. the discussion below and Fig. 7). We note that this is ∼15% thicker than the nominal quoted thickness for our DSAM target, further evidence of the usefulness of comprehensive GEANT4 simulations.

We have also simulated the carbon recoil energy spectra and compared the results to the experimental data to verify the accuracy of our implementation of Coulomb excitation reactions in inverse kinematics. We used the restricted range of DSAM target gold backings from the above investigation as a starting point and found a thickness of 11.5 μm yielded the best agreement between the data and simulated energy distributions, both in terms of the peak location and the general shape. This agreement for ring 1 of the TIP silicon PIN diode array is illustrated in Fig. 7. To remove the effect of contaminant reaction kinematics from the spectra, both the experimental and simulated data were gated on the full-energy line shape of the ^{36}Ar 1970.3-keV transition. The inset of the figure shows the large impact of reducing the gold backing thickness by 2 μm from the optimized value on the simulated energy loss.

Taken together, the agreement between data and simulations illustrated in Figs. 6 and 7 provide a strong validation of the simulation's implementation of stopping powers and inelastic scattering kinematics, which strongly impact the simulated γ-ray line-shape distributions. We therefore proceeded to simulate γ-ray energy line shapes to compare with the experimental data. At each lifetime value, the simulated line shapes were normalized to the area of their experimental counterparts. Only simulated γ rays in coincidence with carbon recoils in rings 1 and 2 of the TIP silicon PIN diode array were considered and, as mentioned above, add-back summing was utilized to replicate the experimental data analysis technique. To maximize the experimental statistics and smooth Poisson fluctuations, we summed the two crystal rings together within each clover; the same was done for the simulations. Then, a χ^2 goodness-of-fit test was conducted by comparing the add-back and suppressed experimental γ-ray spectra with their corresponding normalized simulated line shapes for the Doppler-shift sensitive TIGRESS clovers at 45° and 135°. The normalization energy intervals were [1955,2035] keV and [1900,1990] keV, respectively, for TIGRESS clovers at these angles. The distributions of reduced-χ^2 values from this investigation are shown in Fig. 8. In comparison to Fig. 3, the minima of the distributions are significantly deeper, resulting in a more precise lifetime determination.

Cubic-polynomial fits are superimposed upon the 45° and 135° distributions of reduced-χ^2 values in Fig. 8. We extracted a weighted average lifetime from the minima of the fits. The statistical error was taken in part from the calculated average half width of the cubic polynomials evaluated at

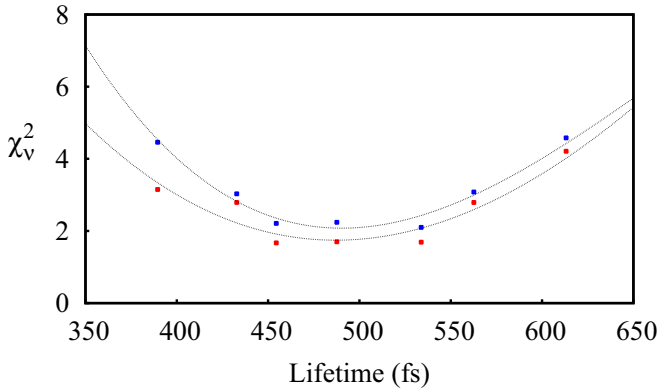

FIG. 8. Distributions of reduced-χ^2 values as a goodness-of-fit test between simulations and experimental data for the forward 45° (red squares) and backward 135° (blue squares) TIGRESS clovers. The distributions have been fit with cubic polynomials to extract the lifetime values.

$\chi^2_\nu = \chi^2_{\nu,\min} + 1/\nu$. The largest of these yielded an uncertainty of 7 fs. To this, we added an additional 8 fs of uncertainty extracted from an investigation of the response of the lifetime in the minimum to reasonable variations in the polynomial fit parameters. Lastly, we included a 10% systematic uncertainty in the SRIM stopping powers. Adding this in quadrature to the 15 fs above, we arrive at a lifetime result of 489 ± 51 fs.

The resulting fit quality of simulations to the experimental TIGRESS spectra for this lifetime result is illustrated in Figs. 9(a)– 9(c), 9(e), and 9(f). A comparison of Figs. 9(c) and 9(d) illustrates the large impact of applying coincident carbon recoil gates in the simulation in a manner consistent with the experimental data. Figure 9(d) clearly exhibits a large Doppler-shift component from very fast projectiles; these correspond to slow carbon recoils which are fully stopped in the gold DSAM target backing. These were not detected experimentally, nor do they appear in the properly gated simulated line shapes. Figures 9(e) and 9(f) illustrate the quality of the fit when the forward TIGRESS clovers of Fig. 9(c) are split into their composite 55° and 35° crystal rings, respectively. Note the difference in the line shape at large Doppler shifts that is accurately reproduced in the simulations. In comparison to the method I simulated line shapes in Figs. 5(c) and 5(d), we note that the corresponding method II simulated line shapes of Figs. 5(e) and 5(f) better match the large Doppler-shift tail of the experimental data and also the low-energy background.

In a manner similar to what was done above, we have also investigated $\mathcal{R}$ as a function of simulated lifetime using the experimental data and normalized simulated line shapes of method II. Figures 10(a) and 10(b) plot $\mathcal{R}$ for the 45° and 135° TIGRESS clover detectors, respectively, with linear best-fit lines and the horizontal $\mathcal{R} = 1$ lines. The blue squares represent $\mathcal{R}$ values calculated from the integration of the stopped peak and shifted plateau over the energy intervals identical to those used for the investigation in method I. To probe the impact of our energy interval choices, we have repeated the investigation with stopped peak and shifted plateau energy intervals of [1960,1978] and [1915,1955] keV (backward

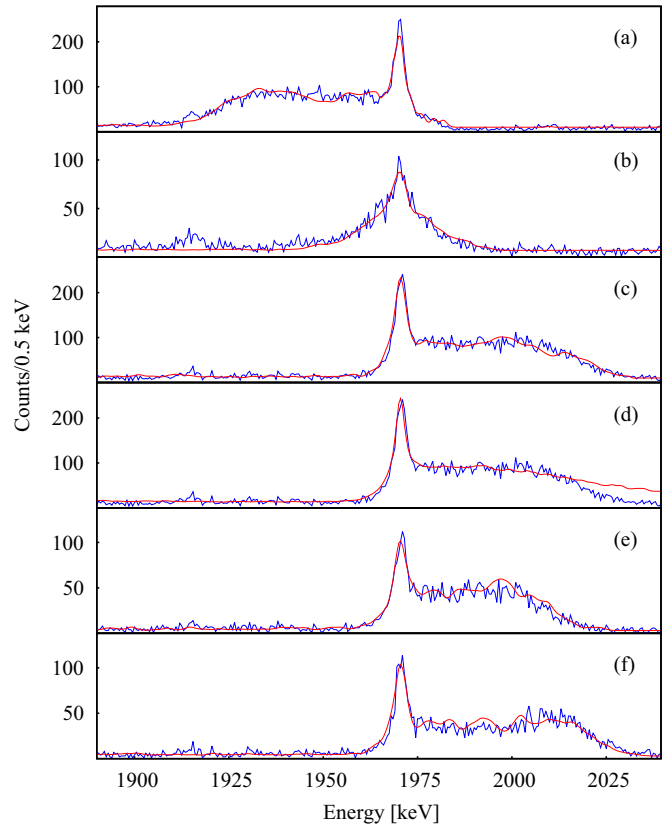

FIG. 9. Experimental (blue) and method II best-fit simulated (red) γ-ray line shapes for the $2^+_1 \rightarrow 0^+_{\text{g.s.}}$ transition in ^{36}Ar for TIGRESS clover detectors at 135° in panel (a), 90° in panel (b), and 45° in panels (c) and (d). The simulations in panels (a)–(c) have an enforced coincident detection of γ rays and carbon recoils detected in rings 1 and 2 of the TIP silicon PIN diode array. For comparison, no such kinematic gate was applied for the simulated line shape in panel (d). Note the contaminant peak near 1915 keV that is not simulated; this is also visible in Fig. 1(c). Panels (e) and (f) are like panel (c), but the comparison between experimental and simulated TIGRESS clover data is split into the two forward TIGRESS rings at 55° and 35°, respectively.

TIGRESS clovers), and [1955,1978] and [1980,2035] keV (forward TIGRESS clovers). These data are shown as red triangles in Fig. 10. We note that the lifetime values intercepting the horizontal $\mathcal{R} = 1$ line are rather insensitive to the energy interval variations; they are within 13 fs of one another in the bottom panel and within 7 fs of one another in the top panel. Moreover, comparing Figs. 4 and 10, we find that the lifetime results are much more consistent between forward and backward TIGRESS clover detectors in our GEANT4 analysis. By averaging the four $\mathcal{R} = 1$ lifetimes and adding in quadrature the largest spread in $\mathcal{R} = 1$ results of 13 fs and a 10% stopping powers uncertainty, we deduce a lifetime of 484 ± 50 fs. This is consistent with the result from the reduced-χ^2 analysis above and provides a valuable self-consistency check while adding credence to our simulations.

Table II summarizes our results alongside shell-model calculations that we have performed using the USDB interaction [53]. This interaction is well constrained in the *sd* model space

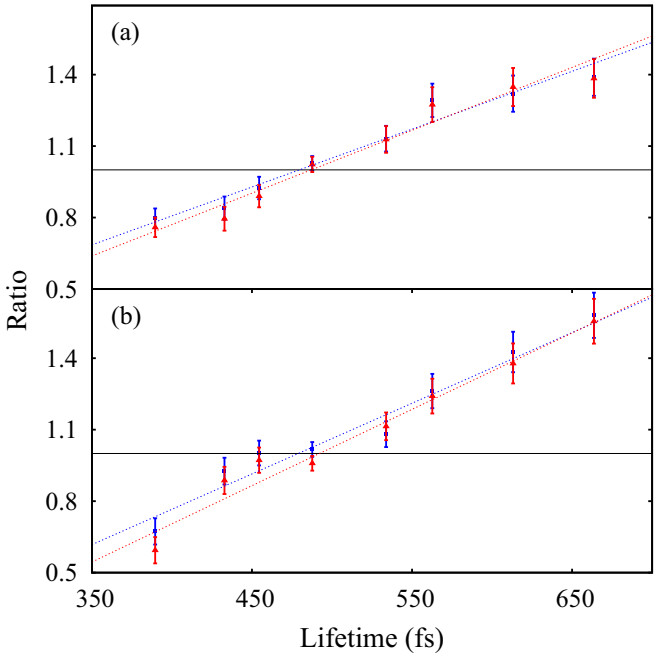

FIG. 10. $\mathcal{R} = \mathcal{R}_{\text{stopped}}/\mathcal{R}_{\text{shifted}}$ as a function of simulated lifetime for the 45° TIGRESS clovers in panel (a) and the 135° TIGRESS clovers in panel (b). The blue squares and red triangles represent $\mathcal{R}$ values calculated using different stopped peak and shifted plateau energy intervals.

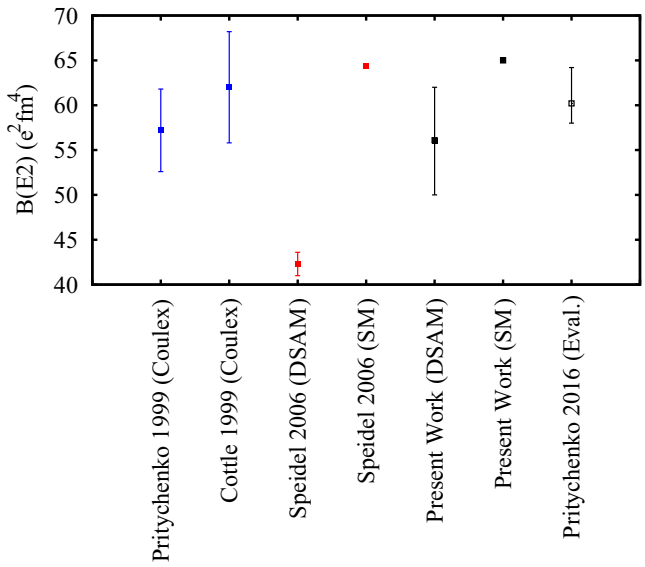

FIG. 11. The $B(E2)$ derived from the lifetime result reported in this work and the associated shell-model calculation (filled black squares) are compared to the adopted model-independent literature value (open black square) of Ref. [54] ("Pritychenko 2016"), the two intermediate energy Coulomb excitation results (filled blue squares) of Ref. [25] ("Pritychenko 1999") and [26] ("Cottle 1999"), and the DSAM result and associated shell-model calculation (filled red squares) of Ref. [27] ("Speidel 2006").

and reproduces the data well throughout this mass region. We note that our method I and II results are in 1σ agreement with one another, but the method II results from the more comprehensive GEANT4 simulations are more self-consistent. Moreover, as no attempt was made to quantify the error of the polynomial fits to the method I χ^2_ν distributions, the method II results are more precise. We therefore adopt a final lifetime result of 490 ± 50 fs from the two significant-figure average of our method II investigations.

This lifetime result yields a reduced quadrupole transition strength of $B(E2; 2^+_1 \rightarrow 0^+_{\text{g.s.}}) = 56 \pm 6\,\text{e}^2\text{fm}^4$, in relatively good agreement with our shell-model calculations as well as the essentially equivalent calculations presented in Table I from Ref. [27]. We remark that the calculated $E(2^+_1)$ of 1818 keV is only roughly 150 keV below the experimental value. As expected, the correspondence between our experimental results and the calculations of low-lying properties in ^{36}Ar is satisfactory without incorporating excitations into the pf model space. In addition, the measurement presented here is in excellent agreement with the intermediate energy Coulomb excitation measurements of Refs. [25,26] as well as the recently adopted model-independent literature value of $B(E2) = 60.2^{+4.0}_{-2.2}\,\text{e}^2\text{fm}^4$ from Ref. [54]. This strongly suggests a resolution to the 2^+_1 lifetime discrepancies reported in the DSAM lifetime measurement of Ref. [27]. A comparison of these three previous measurements with the work presented here, along with the two shell-model calculations and the model-independent literature value, is illustrated in Fig. 11.

TABLE II. Reduced quadrupole transition rate and lifetime values for the first 2^+ excited state in ^{36}Ar taken from the investigations of methods I and II as well as our shell-model calculations. We adopt our final two significant-figure result from the average of the method II lifetime investigations.

Investigation	$B(E2)$ (e^2fm^4)	τ (fs)
Method I $\chi^2_{\nu,\text{min}}$	49.3 ± 5.2	557 ± 58
Method I $\mathcal{R}$	51.6 ± 5.7	532 ± 58
Method II $\chi^2_{\nu,\text{min}}$	56.2 ± 5.9	489 ± 51
Method II $\mathcal{R}$	56.7 ± 5.9	484 ± 50
USDB shell-model calc.	65.0	423

The coincident γ-ray and charged-particle spectroscopy technique presented here improved the signal-to-noise ratio of the γ-ray line-shape signatures, resulting in a precise lifetime determination. This technique will clearly benefit experiments with low-intensity radioactive beams in inverse kinematics. To provide an anticipatory glimpse of its use in such measurements, we conducted two final investigations.

First, the incremental improvement in the precision of our lifetime result—by first kinematic gating on the carbon recoils and then applying digital rise-time discrimination—was assessed. Using the GEANT4 framework of method II, we generated new simulated line shapes at the best-fit lifetime for the 45° TIGRESS clover detectors for the case of carbon-recoil detection in any of the four silicon PIN diode array rings, rather than just the inner two rings. The line shapes were normalized to the corresponding data set [cf. Fig. 1(a)] and the χ^2_ν value of the fit was calculated. The procedure was repeated for the

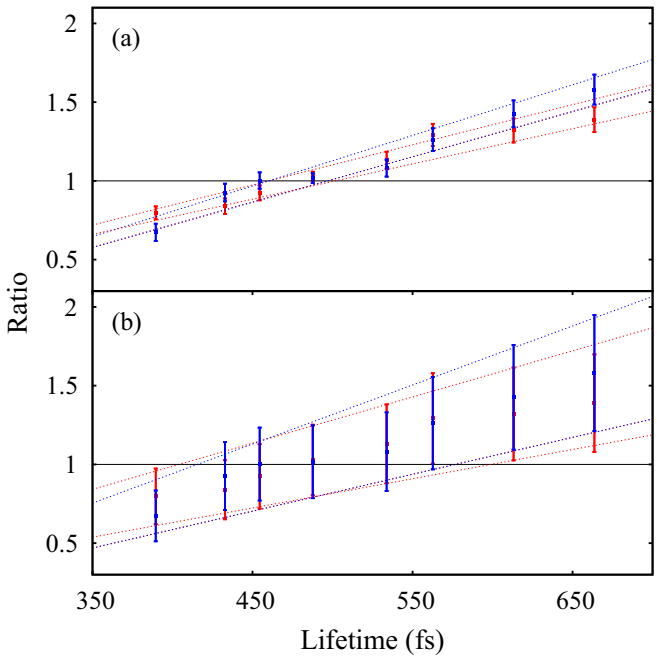

FIG. 12. $\mathcal{R} = \mathcal{R}_{\text{stopped}}/\mathcal{R}_{\text{shifted}}$ as a function of simulated lifetime for the 45° (red squares) and 135° (blue squares) TIGRESS clovers. The data are the same as the blue data of Fig. 10, but the error bars are enlarged due to 20- and 100-fold beam-intensity reductions in panels (a) and (b), respectively. The spread in $\mathcal{R} = 1$ intersections of the best-fit lines for the upper and lower 1σ limits yields a measure of the loss of precision with decreasing experimental statistics.

case of carbon-recoil detection in the innermost two rings, but without digital rise-time discrimination [cf. Fig. 1(b)]. In this case, the best-fit simulations from above, as illustrated in Fig. 9, were renormalized and used since simulating DRD was unnecessary. We determined that the χ^2_ν value of the best fit decreased by 13% due to kinematic gating alone and an additional 14% when using DRD.

The reduction in the best-fit χ^2_ν value demonstrates the improvement in precision via kinematic gating and DRD; this improvement is small due to the high statistics of this stable-beam experiment. We have therefore characterized the dependence of our lifetime precision on experimental statistics using the ratio $\mathcal{R}$. The squared fractional uncertainty of $\mathcal{R}$ is given by the sum of the inverse integrated counts in the stopped peaks and shifted plateaus of the experimental and simulated line shapes. For the case of the 489-fs simulated lifetime, we obtain a fractional uncertainty in $\mathcal{R}$ for the 45° and 135° TIGRESS clover detectors of 2.9% and 3.0%, respectively. These values correspond to the blue 489-fs data and error bars in Fig. 10. For 20- and 100-fold reductions in beam intensity, the experimental statistics were reduced correspondingly, but the simulated statistics remained fixed. For these reductions, we obtained fractional uncertainties of 9.9% and 21.8%, respectively, for the 45° detectors and 10.3% and 22.7%, respectively, for the 135° detectors. Figure 12 reproduces the blue data from Fig. 10 with larger error bars due to these beam-intensity reductions. The linear best-fit lines were calculated from the data at the upper and lower 1σ limits and their $\mathcal{R} = 1$ intersections were noted. An estimate of the decrease in lifetime precision is given by the ratio of the difference in these upper and lower 1σ intersections to their average. Averaging the ratios for the 45° and 135° detectors yielded fractional uncertainties in the lifetime of 17% and 36% for 20- and 100-fold beam-intensity reductions, respectively. This is to be compared with only 8% if we analyze our high-statistics data in the same manner.

IV. CONCLUSION AND OUTLOOK

The TIGRESS Integrated Plunger and its suite of ancillary charged-particle detectors and target systems were designed to provide precision electromagnetic transition rate measurements with the TIGRESS γ-ray spectrometer. Here, we have reported a new DSAM lifetime measurement of the 2^+_1 excited state in ^{36}Ar as the first test of transition rate studies with TIGRESS and the TIP silicon PIN diode array at TRIUMF with beams from the ISAC-II facility. This precision measurement benefited from significant background reduction in the Doppler-shifted γ-ray line shapes through the complementary techniques of kinematic gating and digital rise-time discrimination of recoiling charged particles from the DSAM target in the TIP silicon PIN diode array. The resulting experimental γ-ray line shapes were compared to simulated line shapes generated within the Lindhard formalism as a first-pass analysis, then with more comprehensive Monte Carlo GEANT4 simulations that afforded greater confidence and precision in our results. Through both χ^2 analysis of the fits and a ratio analysis of the stopped and slowing features of the DSAM line shape, we have determined a best-fit lifetime of $\tau(2^+_1) = 490 \pm 50$ fs, corresponding to a reduced quadrupole transition strength of $B(E2; 2^+_1 \rightarrow 0^+_{\text{g.s.}}) = 56 \pm 6$ e^{2}fm^4.

This robust and model-independent result is in agreement with previous intermediate energy Coulomb excitation measurements, thereby resolving the discrepancy between these results and the later DSAM measurement. The measurement is also in relatively good agreement with our *sd* shell-model calculations, without having to invoke cross-shell excitations beyond the $N(Z) = 20$ shell gap into the *pf* model space, as to be expected for this $N = Z = 18$ system. The results presented here motivate further nuclear structure studies with TIP that will benefit from its precision reaction-channel selectivity which enhance TIGRESS γ-ray line-shape signatures, especially those using high-intensity beams to populate weak channels in the presence of large backgrounds. We especially look toward the possibility of near-simultaneous Doppler-shift lifetime and low-energy Coulomb excitation measurements using the same experimental setup to minimize systematic uncertainties. Such investigations can provide direct access to both transition rate and nuclear shape information.

ACKNOWLEDGMENTS

The authors would like to acknowledge the support of the ISAC Operations Group at TRIUMF, the TRIUMF Detectors and Engineering Groups, and the TRIUMF Scintillator Shop as well as the invaluable assistance and expertise of the Simon Fraser University Science Machine and Electronics Shops.

This work is supported by the National Sciences and Engineering Research Council of Canada Awards SAPIN/371656-2010 and SAPEQ/390539-2010 and the Simon Fraser University Vice President, Research. TRIUMF receives federal funding via a contribution agreement from the National Research Council of Canada.

[1] I. Talmi and I. Unna, Phys. Rev. Lett. **4**, 469 (1960).
[2] D. E. Alburger, C. Chasman, K. W. Jones, J. W. Olness, and R. A. Ristinen, Phys. Rev. **136**, B916 (1964).
[3] E. Kwan, C. Y. Wu, N. C. Summers, G. Hackman, T. E. Drake, C. Andreoiu, R. Ashley, G. C. Ball, P. C. Bender, A. J. Boston *et al.*, Phys. Lett. B **732**, 210 (2014).
[4] E. K. Warburton, J. A. Becker, and B. A. Brown, Phys. Rev. C **41**, 1147 (1990).
[5] B. A. Brown, Prog. Part. Nucl. Phys. **47**, 517 (2001).
[6] A. N. Andreyev, M. Huyse, P. Van Duppen, L. Weissman, D. Ackermann, J. Gerl, F. P. Hessberger, S. Hofmann, A. Kleinböhl, G. Münzenberg *et al.*, Nature (London) **405**, 430 (2000).
[7] H. Mei, J. Xiang, J. M. Yao, Z. P. Li, and J. Meng, Phys. Rev. C **85**, 034321 (2012).
[8] J. Xiang, Z. P. Li, Z. X. Li, J. M. Yao, and J. Meng, Nucl. Phys. A **873**, 1 (2012).
[9] K. Starosta, A. Dewald, A. Dunomes, P. Adrich, A. M. Amthor, T. Baumann, D. Bazin, M. Bowen, B. A. Brown, A. Chester *et al.*, Phys. Rev. Lett. **99**, 042503 (2007).
[10] A. Obertelli, T. Baugher, D. Bazin, J.-P. Delaroche, F. Flavigny, A. Gade, M. Girod, T. Glasmacher, A. Goergen, G. F. Grinyer *et al.*, Phys. Rev. C **80**, 031304 (2009).
[11] A. J. Nichols, R. Wadsworth, H. Iwasaki, K. Kaneko, A. Lemasson, G. de Angelis, V. M. Bader, T. Baugher, D. Bazin, M. A. Bentley *et al.*, Phys. Lett. B **733**, 52 (2014).
[12] A. Gade, D. Bazin, A. Becerril, C. M. Campbell, J. M. Cook, D. J. Dean, D.-C. Dinca, T. Glasmacher, G. W. Hitt, M. E. Howard *et al.*, Phys. Rev. Lett. **95**, 022502 (2005).
[13] A. Lemasson, H. Iwasaki, C. Morse, D. Bazin, T. Baugher, J. S. Berryman, A. Dewald, C. Fransen, A. Gade, S. McDaniel *et al.*, Phys. Rev. C **85**, 041303 (2012).
[14] P. Voss, R. Henderson, C. Andreoiu, R. Ashley, R. A. E. Austin, G. C. Ball, P. C. Bender, A. Bey, A. Cheeseman, A. Chester *et al.*, Nucl. Instrum. Methods A **746**, 87 (2014).
[15] T. K. Alexander and J. S. Forster, in *Advances in Nuclear Physics, Volume 10*, edited by M. Baranger and E. Vogt (Plenum Press, New York, 1978), Chap. 3.
[16] A. Dewald, O. Möller, and P. Petkov, Prog. Part. Nucl. Phys. **67**, 786 (2012).
[17] K. Alder and A. Winther, *Electromagnetic Excitation: Theory of Coulomb Excitation with Heavy Ions* (Elsevier, Amsterdam, 1975).
[18] H. C. Scraggs, C. J. Pearson, G. Hackman, M. B. Smith, R. A. E. Austin, G. C. Ball, A. J. Boston, P. Bricault, R. S. Chakrawarthy, R. Churchman *et al.*, Nucl. Instrum. Methods A **543**, 431 (2005).
[19] C. E. Svensson, G. Hackman, C. J. Pearson, M. A. Schumaker, H. C. Scraggs, M. B. Smith, C. Andreoiu, A. Andreyev, R. A. E. Austin, G. C. Ball *et al.*, Nucl. Instrum. Methods A **540**, 348 (2005).
[20] C. E. Svensson, P. Amaudruz, C. Andreoiu, A. Andreyev, R. A. E. Austin, G. C. Ball, D. Bandyopadhyay, A. J. Boston, R. S. Chakrawarthy, A. A. Chen *et al.*, J. Phys. G: Nucl. Part. **31**, S1663 (2005).
[21] G. Hackman and C. E. Svensson, Hyperfine Interact. **225**, 241 (2014).
[22] W. Rother, A. Dewald, G. Pascovici, C. Fransen, G. Frießner, M. Hackstein, G. Ilie, H. Iwasaki, J. Jolie, and B. Melon *et al.*, Nucl. Instrum. Methods A **654**, 196 (2011).
[23] J. Williams, C. Andreoiu, R. Ashley, G. C. Ball, T. Ballast, P. C. Bender, C. Bolton, V. Bildstein, A. Chester, D. S. Cross *et al.*, Nucl. Instrum. Methods A **859**, 8 (2017).
[24] T. Glasmacher, Annu. Rev. Nucl. Part. Sci. **48**, 1 (1998).
[25] B. V. Pritychenko, T. Glasmacher, P. D. Cottle, M. Fauerbach, R. W. Ibbotson, K. W. Kemper, V. Maddalena, A. Navin, R. Ronningen, and A. Sakharuk *et al.*, Phys. Lett. B **461**, 322 (1999).
[26] P. D. Cottle, M. Fauerbach, T. Glasmacher, R. W. Ibbotson, K. W. Kemper, B. V. Pritychenko, H. Scheit, and M. Steiner, Phys. Rev. C **60**, 031301 (1999).
[27] K.-H. Speidel, S. Schielke, J. Leske, J. Gerber, P. Maier-Komor, S. J. Q. Robinson, Y. Y. Sharon, and L. Zamick, Phys. Lett. B **632**, 207 (2006).
[28] S. Raman, C. H. Malarkey, W. T. Milner, C. W. Nestor, and P. H. Stelson, At. Data Nucl. Data **36**, 1 (1987).
[29] A. A. Lis, C. Mazzocchi, W. Dominik, Z. Janas, M. Pfützner, M. Pomorski, L. Acosta, S. Baraeva, E. Casarejos, J. Duénas-Díaz *et al.*, Phys. Rev. C **91**, 064309 (2015).
[30] R. Winkler, A. Gade, T. Baugher, D. Bazin, B. A. Brown, T. Glasmacher, G. F. Grinyer, R. Meharchand, S. McDaniel, A. Ratkiewicz *et al.*, Phys. Rev. Lett. **108**, 182501 (2012).
[31] D. Steppenbeck, S. Takeuchi, N. Aoi, P. Doornenbal, M. Matsushita, H. Wang, Y. Utsuno, H. Baba, S. Go, J. Lee *et al.*, Phys. Rev. Lett. **114**, 252501 (2015).
[32] H. Scheit, T. Glasmacher, B. A. Brown, J. A. Brown, P. D. Cottle, P. G. Hansen, R. Harkewicz, M. Hellström, R. W. Ibbotson, J. K. Jewell *et al.*, Phys. Rev. Lett. **77**, 3967 (1996).
[33] A. Gade, D. Bazin, C. M. Campbell, J. A. Church, D. C. Dinca, J. Enders, T. Glasmacher, Z. Hu, K. W. Kemper, and W. F. Mueller *et al.*, Phys. Rev. C **68**, 014302 (2003).
[34] S. Calinescu, L. Cáceres, S. Grévy, O. Sorlin, D. Sohler, M. Stanoiu, F. Negoita, E. Clément, R. Astabatyan, and C. Borcea *et al.*, Acta Phys. Pol. B **45**, 199 (2014).
[35] Z. Meisel, S. George, S. Ahn, J. Browne, D. Bazin, B. A. Brown, J. F. Carpino, H. Chung, R. H. Cyburt, A. Estradé *et al.*, Phys. Rev. Lett. **114**, 022501 (2015).
[36] C. E. Svensson, A. O. Macchiavelli, A. Juodagalvis, A. Poves, I. Ragnarsson, S. Åberg, D. E. Appelbe, R. A. E. Austin, C. Baktash, G. C. Ball *et al.*, Phys. Rev. Lett. **85**, 2693 (2000).
[37] C. E. Svensson, A. O. Macchiavelli, A. Juodagalvis, A. Poves, I. Ragnarsson, S. Åberg, D. E. Appelbe, R. A. E. Austin, G. C. Ball, and M. P. Carpenter *et al.*, Phys. Rev. C **63**, 061301 (2001).

[38] E. Caurier, F. Nowacki, and A. Poves, Phys. Rev. Lett. **95**, 042502 (2005).
[39] A. F. Lisetskiy, E. Caurier, K. Langanke, G. Martínez-Pinedo, P. von Neumann-Cosel, F. Nowacki, and A. Richter, Nucl. Phys. A **789**, 114 (2007).
[40] R. E. Laxdal, Nucl. Instrum. Methods B **204**, 400 (2003).
[41] J. Greene, P. Voss, and K. Starosta, J. Radiol. Nucl. Chem. **299**, 1121 (2014).
[42] M. A. Schumaker, G. Hackman, C. J. Pearson, C. E. Svensson, C. Andreoiu, A. Andreyev, R. A. E. Austin, G. C. Ball, D. Bandyopadhyay, A. J. Boston *et al.*, Nucl. Instrum. Methods A **570**, 437 (2007).
[43] J.-P. Martin, C. Mercier, N. Starinski, C. J. Pearson, and P.-A. Amaudruz, IEEE Trans. Nucl. Sci. **55**, 84 (2008).
[44] M. A. Schumaker, C. E. Svensson, C. Andreoiu, A. Andreyev, R. A. E. Austin, G. C. Ball, D. Bandyopadhyay, A. J. Boston, R. S. Chakrawarthy, R. Churchman *et al.*, Nucl. Instrum. Methods A **573**, 157 (2007).
[45] P. Voss, R. Henderson, C. Andreoiu, R. Ashley, G. C. Ball, P. C. Bender, A. Chester, D. S. Cross, T. E. Drake, and A. B. Garnsworthy *et al.*, Phys. Proced. **66**, 524 (2015).
[46] J. Cameron, J. Chen, B. Singh, and N. Nica, Nucl. Data Sheets **113**, 365 (2012).
[47] W. M. Currie, Nucl. Instrum. Methods **73**, 173 (1969).
[48] J. F. Ziegler, M. Ziegler, and J. Biersack, Nucl. Instrum. Methods B **268**, 1818 (2010).
[49] D. Cullen (private communication).
[50] S. Agostinelli, J. Allison, K. Amako, J. Apostolakis, H. Araujo, P. Arce, M. Asai, D. Axen, S. Banerjee, G. Barrand *et al.*, Nucl. Instrum. Methods A **506**, 250 (2003).
[51] L. Urban, CERN-OPEN-2006-077, GEANT4 Associates International Ltd., U.K. 2006 (unpublished).
[52] O. Wieland, F. Camera, B. Million, A. Bracco, and J. van der Marel, Nucl. Instrum. Methods A **487**, 441 (2002).
[53] B. A. Brown and W. A. Richter, Phys. Rev. C **74**, 034315 (2006).
[54] B. Pritychenko, M. Birch, B. Singh, and M. Horoi, At. Data Nucl. Data Tables **107**, 1 (2016).